JGR Space Physics

RESEARCH ARTICLE
10.1029/2025JA033792

Magnetosheath Jet-Triggered ULF Waves: Energy Deposition in the Ionosphere

E. Krämer[1], M. Hamrin[1], H. Gunell[1], L. Baddeley[2], N. Partamies[2], S. Raptis[3], K. Herlingshaw[2], and A. Schillings[1]

[1]Departement of Physics, Umeå University, Umeå, Sweden, [2]Department of Arctic Geophysics, University Centre in Svalbard, Longyearbyen, Norway, [3]Johns Hopkins University Applied Physics Laboratory, Laurel, MD, USA

Key Points:

- Joule heating rate from magnetosheath jet-triggered ultralow frequency (ULF) waves and FLRs are comparable
- Jet-triggered ULF waves are on average not relevant to the magnetospheric energy budget
- Simultaneous observations of jet-triggered ULF waves and enhanced auroral precipitation

Correspondence to:
E. Krämer,
eva.kramer@umu.se

Citation:
Krämer, E., Hamrin, M., Gunell, H., Baddeley, L., Partamies, N., Raptis, S., et al. (2025). Magnetosheath jet-triggered ULF waves: Energy deposition in the ionosphere. *Journal of Geophysical Research: Space Physics*, *130*, e2025JA033792. https://doi.org/10.1029/2025JA033792

Received 27 JAN 2025
Accepted 8 APR 2025

Abstract Magnetosheath jets, transient plasma structures of enhanced dynamic pressure, have been observed to trigger ultra-low frequency (ULF) waves in the magnetosphere. These ULF waves contribute to energy transport in the magnetosphere-ionosphere system. Therefore, there is a need to estimate the energy input into the ionosphere due to jet-triggered ULF waves. In this study, we combine measurements from Magnetospheric Multiscale, ground-based magnetometers, the EISCAT radar on Svalbard, and SuperDARN to estimate the Joule heating in the ionosphere resulting from jet impacts at the magnetopause. Focusing on three jets observed on 2016-01-07 we were able to calculate the Joule heating for two jets. We found an average Joule heating rate of 0.38 mW/m^2 which is on par with other processes such as field line resonances. However, due to the short duration and spatial confinement of the jet-induced ULF waves, the average energy input was only $9 \cdot 10^{10}$ J. This suggests that the energy deposition of jet-triggered ULF waves is small compared to other magnetospheric processes, and thus does not significantly impact the average energy budget of the magnetosphere.

Plain Language Summary The solar wind is a supersonic plasma flow that forms the bow shock when interacting with Earth. At this bow shock the incoming solar wind plasma is heated and slowed down, forming the magnetosheath. Sometimes, dynamic pressure enhancements are found in the magnetosheath, so-called magnetosheath jets. These jets can cause localized disturbances in the Earth magnetic field. The disturbance can propagate as a wave along the magnetic field into the ionosphere, the upper ionized part of the atmosphere. In this work we investigate the energy input in the ionosphere due to these jet-triggered waves. We find that the energy input is small compared to other processes in the magnetosphere.

1. Introduction

The Earth's plasma environment is affected by the Sun's varying energy deposit into our planetary environment. One process that deposits energy is magnetosheath jets—dense, fast-moving plasma structures (e.g., Krämer et al., 2025; Plaschke et al., 2018). Those jets trigger low frequency waves in the magnetosphere (Norenius et al., 2021; Wang et al., 2018). However, the energy input in the ionosphere through such jet-triggered waves remains unknown. Such an energy estimate requires the use of multiple instruments to determine the Poynting flux, the affected area, and the duration of the event.

The Sun is the source a continuous plasma flow, the solar wind, carrying energy from the Sun into space. When the solar wind interacts with Earth, the bow shock forms due to the solar winds supersonic nature. At this shock, magnetosheath jets can form through different generation mechanisms (see review by Plaschke et al. (2018) for an overview). These jets propagate through the magnetosheath and can subsequently impact the magnetopause and deform it (Escoubet et al., 2020; Shue et al., 2009). Local deformations caused by magnetosheath jets can launch ultra low frequency (ULF) waves in the magnetosphere (Norenius et al., 2021; Wang et al., 2022). Due to the initial compression of the magnetopause, compressional waves are launched which couple to Alfvén waves. These Alfvén waves then propagate along the magnetic field into the ionosphere causing localized disturbances in the magnetic field. These waves are therefore a source of energy.

Magnetosheath jets are transient phenomena, but their cumulative effect must be taken into account. The occurrence rate of jets mainly depends on the orientation of the bow shock normal with respect to the interplanetary magnetic field (IMF). The angle between the bow shock normal and the IMF is θ_{Bn} which is often used to characterize the local bow shock. The bow shock is quasi-parallel when $\theta_{Bn} < 45°$ and quasi-perpendicular

when $\theta_{Bn} > 45°$. Generally, the observation rate of jets increases with decreasing θ_{Bn} and an increased occurrence is therefore associated with the quasi-parallel bow shock (Plaschke et al., 2013; Vuorinen et al., 2019). A lower θ_{Bn} causes more jets which will impact the magnetopause more often (Plaschke et al., 2020). More magnetopause impacts lead to more energy deposition over time.

Similarly to the bow shock, the downstream magnetosheath can also be classified as quasi-parallel and quasi-perpendicular. The plasma in the quasi-parallel magnetosheath originates from the quasi-parallel bow shock. The quasi-parallel magnetosheath exhibits more magnetic field fluctuations compared to the quasi-perpendicular magnetosheath (Luhmann et al., 1986). In addition, the quasi-parallel magnetosheath contains more high energetic ions (ranging from a few keV/e up to 150 keV/e (Fuselier, 1994)) compared to the quasi-perpendicular magnetosheath.

After the jets' generation at the bow shock, they propagate through the magnetosheath and reach the magnetopause frequently (Plaschke et al., 2016, 2020). Generally, the median scale size of jets is of the order of 0.1 R_E (Plaschke et al., 2020). However, jets with a large spatial extent are thought to cause larger deformations of the magnetopause and therefore have a larger impact on the magnetospheric-ionospheric system. These jets are then considered to be geoeffective. Plaschke et al. (2020) found that large jets with a cross-sectional diameter larger than 2 Earth radii ($R_E = 6371$ km) impact the magnetopause at rates of 7.9/h during low angles between the Earth-Sun line and the IMF ($<30°$) as compared to 2.4/hr overall. The magnetopause has also been suggested to act as a low-pass filter suppressing disturbances with time scales smaller than a few minutes (Archer et al., 2013). When studying the geoeffectivness of jets it is therefore natural to focus on larger jets.

Jets have been suggested to be geoeffective through different processes (Plaschke et al., 2018). One process is ULF waves in the Pc5 frequency range (1.67−6.67 mHz), corresponding to 150−600 s wave periods (Archer et al., 2013; Hietala et al., 2012; Norenius et al., 2021; Wang et al., 2022). Hietala et al. (2012) associated both irregular pulsations at the geostationary orbit as well localized flow enhancements in the ionosphere with jets. Similarly, Archer et al. (2013) reported waves which were induced by jets using satellite measurements in the magnetosphere and ground-magnetometers. Jet-triggered ULF waves were statistically investigated by Norenius et al. (2021) and Wang et al. (2022). Norenius et al. (2021) studied 65 magnetosheath jets and their ground response. The authors found that the average magnetic field disturbance has an amplitude of 34 nT, the average frequency is 1.9 mHz, and the average damping time is 370 s. The authors also investigated the time delay between the detection of the jet in the magnetosheath and the ground response which they estimated to be 190 s. Wang et al. (2022) studied 644 jets whereof 37% triggered ground oscillations with periods of 150−700 s. For jets observed close to the magnetopause, the likelihood of triggering ground oscillations increases to 50%. The authors then separated their database into isolated jets and recurring jets. They found that recurring jets generally exhibit a larger wave power compared to isolated jets.

Jets have also been associated with optical signatures, such as the brightening of discrete and diffuse aurora (Wang et al., 2018). In the investigated cases, the auroral brightening showed similarities with shock aurora, but with a smaller extent. The authors suggested that field-aligned currents and the associated field-aligned electric fields cause particle acceleration and lead to the auroral brightening.

Pc5 waves can generally be divided into two classes, poloidal-mode waves and toroidal-mode waves. Poloidal-mode waves exhibit radial magnetic-field perturbations and these waves usually have large azimuthal wave numbers m (small azimuthal scale size). Waves with large azimuthal wave numbers are highly attenuated by the ionosphere, making them difficult to study with ground magnetometers (Yeoman et al., 2000). In this paper we will use ground-magnetometers to study Pc5 waves, which therefore refers the toroidal-mode waves with small m (large azimuthal scale sizes) and azimuthal magnetic field perturbations.

Dayside Pc5 waves are known to be excited through a range of processes. Commonly, sources are thought to be the solar wind, instabilities at the magnetopause, as well as interactions inside the magnetosphere (see Menk (2011) for an overview). In the solar wind, dynamic pressure oscillations (such as those associated with jets) have been found to be a major driver for Pc5 waves. For example, Kessel (2008) reported that over 80% of the Pc5 activity in the magnetosphere is driven by dynamic pressure fluctuations and less than 20% are attributed to interaction processes internal to the magnetosphere.

Ultralow frequency waves are known to transport energy into the ionosphere. Rae et al. (2007) estimated the energy deposition in the ionosphere for a global field line resonance (FLR), a standing mode ULF oscillation. The

authors assumed that all energy is dissipated via Joule heating. During a 3 hr time interval the authors estimated that 30% energy of a substorm was dissipated in the ionosphere via Joule heating. The authors therefore concluded that ULF waves can be a major energy source for magnetospheric processes.

Norenius et al. (2021) and Wang et al. (2022) suggested that jets are an important source of ULF waves that can disturb the magnetospheric-ionospheric system. However, these studies have not calculated the energy input through jet-triggered ULF waves in the ionosphere. To make a qualitative assessment of the importance of jet-triggered ULF waves, an estimate of that energy input is needed. To our knowledge, no such estimate exists. We therefore aim to estimate the energy input in the ionosphere by jet-triggered ULF waves. We then compare this estimate to other known processes that dissipate energy in the ionosphere to quantify the importance of jets for the magnetospheric-ionospheric energy budget. In order to estimate the energy input, we assess the duration, disturbed area on the ground, and the resulting Joule heating in the ionosphere. We use the Joule heating as a proxy for the Poynting flux. Usually, jet-triggered disturbances are assumed to be localized, affecting only a small surface area on Earth (Norenius et al., 2021; Wang et al., 2022). However, it is important to consider the entire disturbed area in order to estimate the energy input.

The paper is structured as follows, in Section 2 we give an overview of the instrumentation and methods. Section 3 investigates the ground-impact of three magnetosheath jets on 2016-01-07 and estimates the disturbed area on the ground. In Section 4 we estimate the Joule heating for two of the three jets. In Section 5 we discuss our results and compare our model with observations.

2. Instrumentation and Methods

All spacecraft data are presented in the Geocentric solar magnetospheric (GSM) coordinate system if not specified otherwise. Coordinates on the ground are given in magnetic latitude (MLAT) and magnetic longitude (MLON) in altitude-adjusted corrected geomagnetic coordinates (AACGM) (Burrell et al., 2023; Shepherd, 2014) on 2016-01-07. We furthermore converted MLON to magnetic local time (MLT). Data from ground magnetometers is presented in a local coordinate system where B_N is the north-south component, B_E the east-west component, and B_Z the vertical down component. For modeled data we use the same coordinate systems.

2.1. Magnetospheric Model

To model the ground impact of magnetosheath jets, we used the magnetosphere model developed by Tsyganenko (1995, 1996) (referred to as the T96 model). In addition, we estimated the footpoints of jets observed in the magnetosheath with the T96 model. The model depends on the solar wind dynamic pressure $P_d = m_i n v^2$, with the ion mass m_i, solar wind plasma density n, and the solar wind velocity v. Furthermore, IMF B_y and IMF B_z as well as the disturbed storm (Dst) index (Nose et al., 2015b; Sugiura, 1963) are inputs for the T96 model. Given these input parameters, the T96 model outputs an external magnetic field. This external magnetic field represents the magnetopause current, ring current, tail current sheet, the region 1 and 2 field-aligned currents as well as partial penetration of the IMF into the magnetosphere. The external magnetic field can then be added to an internal magnetic field, the Earth magnetic field. We used the International Geomagnetic Reference field (IGRF 13) as a model for the internal Earth magnetic field (Alken et al., 2021).

We demonstrate how we modeled the ground impact area with an artificial jet of radius 1 R_E impacting the magnetopause. The disturbed area on the ground was defined as the area that is connected along the magnetic field to the impact area of the jet at the magnetopause. We call this area on the ground the modeled footarea. The modeled cross section of the jet at the magnetopause is visualized in Figure 1a. Every modeled point (crosses in Figure 1a) on this circle was propagated toward the magnetopause until its position connected to the first field line connecting to the northern ionosphere. We used the following input parameters for the T96 model $n = 4$ cm^{-3}, $v = -550$ km/s, $m_i = 1.94 \cdot 10^{-27}$ kg, Dst $= -22$ nT, $B_y = 3$ nT, and $B_z = -2$ nT (these parameters are similar to the solar wind conditions of the later investigated event). We assumed the solar wind velocity is solely in the x-direction. Furthermore, m_i was chosen assuming 5% alpha particles in the solar wind and protons otherwise. We modeled the response using the IGRF coefficients on 2016-01-07 00:00UT. Figure 1b shows the footarea which encircles an area of $3.8 \cdot 10^{10}$ m^2.

In Figure 1 we highlighted five locations (colored crosses) which were traced from their magnetopause location (Figure 1a) along the magnetic field to the ground (Figure 1b). The center of the impact area on the magnetopause

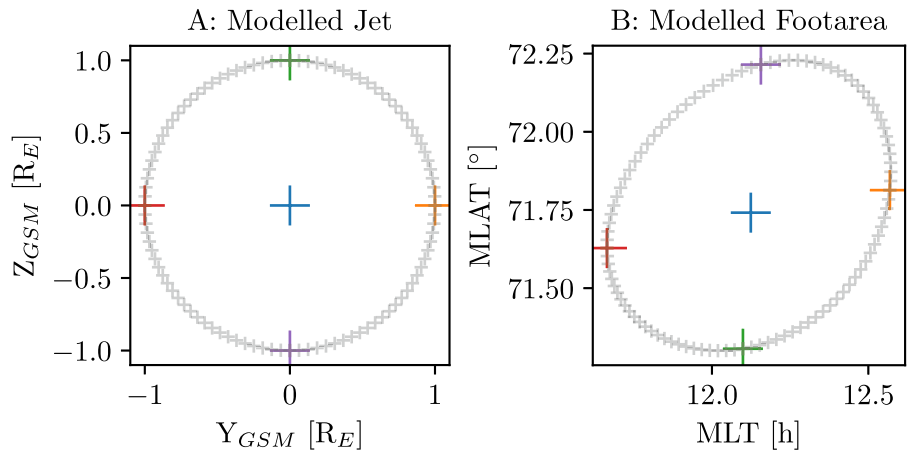

Figure 1. The modeled jet impact using the T96 model with $n_i = 4$ cm^{-3}, $v_i = -550$ km/s, $m_i = 1.94 \cdot 10^{-27}$ kg, Dst $= -22$ nT, $B_y = 3$ nT, and $B_z = -2$ nT. (a) Shape of impacting magnetosheath jets located at the magnetopause nose, and (b) footarea. The footpoints marked as colored crosses in B, C, and D magnetically connect to the highlighted impact points at the magnetopause marked in (a).

(blue cross in Figure 1a) was also located in the center of the footarea (blue crosses in Figure 1b). The jet's impact point at $(x, -1, 0)$ (red cross in Figure 1a) and at $(x, 1, 0)$ (orange cross in Figure 1a) marked the largest extent in y. The jet's impact point at $(x, 0, 1)$ (green cross in Figure 1a) and $(x, 0, -1)$ (purple cross in Figure 1a) correspond to the jet's extent in z. Even though the impact area at the magnetopause is a circle of constant radius of 1 R_E, it maps to a far wider distance longitudinally than latitudinally in the ionosphere.

2.2. Data

We investigated three jets on 2016-01-07 5:45–07:30 UT combining data from spacecraft and ground-based measurements. The instrumentation is introduced in this section.

We used data from the Magnetospheric Multiscale (MMS) mission (Burch et al., 2016) for the detection of jets in the magnetosheath. Fast mode data from the Fluxgate Magnetometer (FGM) (Russell et al., 2016) were used for the magnetic field vector with a sampling rate of 16 Hz. In addition, we used fast mode data from the Fast Plasma Investigation (FPI) (Pollock et al., 2016) for the ion distribution and the provided moments of the distributions. The fast mode FPI data have a sampling rate of 0.25 Hz. We only used data from the MMS1 spacecraft due to the small distance between the spacecraft compared to the size of magnetosheath jets.

For the IMF and solar wind properties we used 1 min high resolution OMNI data propagated to the bow shock nose (Papitashvili & King, 2020). We also used data from the FGM (Auster et al., 2008) on the Time History of Events and Macroscale Interactions during Substorms (THEMIS) C spacecraft (Angelopoulos, 2009) as an additional upstream monitor for the IMF.

In addition, we used data from ground-based magnetometers (GMAGs) obtained from the SuperMAG collaboration (Gjerloev, 2009, 2012). The data have a time resolution of 1 min with daily and yearly baselines removed. In order to investigate Pc5 ULF waves we band-pass filtered the data for the Pc5 frequency range (6.66 − 1.66 mHz). The stations used are given in Table 1 together with their location in geographic and magnetic coordinates.

Ionospheric parameters were measured by the Super Dual Auroral radar network (SuperDARN) (Greenwald et al., 1995) and European Incoherent Scatter (EISCAT) radar on Svalbard. The SuperDARN radar network consists of over 30 HF radars which make observations of the F-region ionospheric convection velocity $(v_E \times B)$. Subsequently, estimates of the local convection electric field can be derived. In this study we use the SuperDARN derived electric field only when calculated directly from the fitted $v_E \times B$ (i.e., only regions where there was backscatter detected by a radar). In particular, we use the 2D convection maps derived from the SuperDARN radars (Ruohoniemi & Baker, 1998) which used the virtual height model developed by Chisham et al. (2008), assuming a maximum virtual height of 400 km (i.e., the scatter is assumed to be ionospheric F-region). The assumed location of scattered signal is converted to AACGM coordinates taking into account different magnetic

Table 1
SuperMAG Stations With Their Positions in the Geographic and Geomagnetic Coordinate System

Station	GLON [°]	GLAT [°]	MLON [°]	MLAT [°]
NAL	11.9	78.9	107.4	76.4
LYR	15.8	78.2	108.7	75.5
HOP	25.0	76.5	112.6	73.4
BJN	19.2	74.5	105.8	71.7
HRN	15.6	77.0	106.5	74.4
BBG	14.2	78.1	107.3	75.5
KUV	302.8	74.6	39.5	79.9
STF	309.3	67.0	39.5	71.8
UPN	303.9	72.8	38.2	78.1
JAN	351.3	70.9	80.8	70.0
DMH	341.4	76.8	81.4	77.0
CBB	255.0	69.1	−45.8	76.4
GDH	306.5	69.2	37.8	74.4
ATU	306.4	67.9	36.8	73.1
SKT	307.1	65.4	36.1	70.5
ABK	18.8	68.3	100.3	65.4
SOR	22.2	70.5	104.5	67.5
SPG	29.7	60.5	105.9	57.0
MOS	37.3	55.5	111.5	51.7
NOR	25.8	71.1	107.8	68.0
HAN	26.6	62.2	103.7	58.8
MNK	27.9	54.5	102.6	50.5
SOD	26.6	67.4	106.1	64.1
TAR	26.5	58.3	102.3	54.6
MAS	23.7	69.5	105.0	66.4
MUO	23.5	68.0	103.9	64.9
TRO	18.9	69.7	101.3	66.8
LOZ	35.0	68.0	113.5	64.6
PEL	24.1	66.9	103.7	63.7
MEK	31.0	62.8	107.7	59.3
KIR	20.4	67.8	101.3	64.8
NR2	24.6	60.5	101.4	57.0
NUR	24.6	60.5	101.4	57.0
KEV	27.0	69.8	107.9	66.6
OUJ	27.2	64.5	105.2	61.2
IVA	27.3	68.6	107.3	65.3

coordinates for different altitudes of the scattered signal. The data have a time resolution of 2 min. The electric field estimates were taken within 5° MLAT and 2° MLON. Density and temperature measurements made by the EISCAT Svalbard radar (Wannberg et al., 1997) were combined with the NRLMSIS atmospheric model (Picone et al., 2002) to produce estimates of the ionospheric Pedersen conductivity at a 1 min time resolution.

2.3. Methods

In this section we describe the identification criteria for jets as well as our method to track jets to the magnetopause. We also describe how we modeled the jets' footpoint. The estimate of the jets' footpoint is similar to the method employed by Norenius et al. (2021).

In the magnetosheath, jets were identified using the criteria proposed by Archer and Horbury (2013). The threshold for jet detection was set to twice the dynamic pressure averaged over a 20 min interval $\langle P_d \rangle_{20\text{min}}$ such that $P_d > 2\langle P_d \rangle_{20\text{min}}$.

In order to estimate the jet's impact point at the magnetopause, we propagated the jet's position in the magnetosheath toward the magnetopause with the jet's velocity during its peak dynamic pressure. This was done with 1 s time steps until the propagated positions connected to a field line connecting to the northern hemisphere using the T96 model. The position of that field line at a radial distance 1 R_E from the Earth's center was considered as the jet's footpoint. For the T96 model input we used solar wind data that was averaged over 10 min centered around the jet's peak dynamic pressure. The averaging evens out possible small scale variations that are of time scales shorter than Pc5 waves. The averaging also takes into account uncertainties in the OMNI propagation time (Case & Wild, 2012; Mailyan et al., 2008).

We also investigated how the ground disturbance varies along approximately constant MLON and constant MLAT from the estimated footpoint. Along approximately constant longitude, we investigated stations that lie within ±0.67 MLT (±10° MLON) of the footpoint and within 50−80° MLAT. At lower latitudes no perturbation contributing significantly to Joule heating is expected but the chosen range allows to examine the characteristics of the perturbation. Along approximately constant MLAT, we investigated data from stations that lie north of the magnetometer station JAN (69.97° MLAT) and below 80° MLAT.

The energy input in the ionosphere was estimated following the method by Rae et al. (2007). The authors estimated the energy input into the ionosphere from a FLR using GMAGs. The authors based their work on Hughes and Southwood (1976) who showed that shielding of ULF waves by Pedersen currents can be expressed as a magnetic perturbation

$$B = \mu_0 \Sigma_p E, \tag{1}$$

where μ_0 is the permittivity of free space, Σ_p is the height integrated Pedersen conductivity, and E is the ionospheric electric field. Assuming that the incoming energy from the Poynting flux is only dissipated through Joule heating due to Pedersen currents in the ionosphere, Equation 1 can be used to express the Poynting flux as

$$\frac{EB}{\mu_0} = \Sigma_p E^2. \tag{2}$$

Integrating over the area and the duration of the ULF waves gives an estimate of the Joule heating in the ionosphere. We then use the Joule heating as a proxy for the energy deposition in the ionosphere.

3. Observations

Here we present data at 2016-01-07 05:45–07:30 UT that will be investigated in more detail. During this time interval multiple jets were observed in the magnetosheath. Three of these jets were associated with ULF wave activity on the ground and those were investigated in more detail. We also studied the spatial extend of the ULF wave activity with ground magnetometers.

An overview of the data is given in Figure 2 which shows data from the MMS 1 spacecraft, OMNI database, THEMIS C spacecraft, GMAGs, SuperDARN, and EISCAT. During that time the MMS1 spacecraft was located inside the magnetosheath at [10,−4.5,−1.2] R_E and the THEMIS C spacecraft was located at [50,−33,3.5] R_E in the solar wind. Figure 2a shows the IMF from the OMNI database propagated to the bow shock nose. Figure 2b shows the IMF measured by the THEMIS C spacecraft. Both IMF measurements show a variable IMF with multiple rotations. Figure 2c shows the solar wind density (red) and solar wind speed (blue) from the OMNI database. The solar wind density varied up to 50% and the solar wind speed varied less than 10% (about 50 km/s). Figure 2d shows the dynamic pressure P_d from the MMS spacecraft located in the magnetosheath as well as $2\langle P_d \rangle_{20\text{min}}$ (threshold for jet detection). The local dynamic pressure exceeded that threshold multiple times during the displayed interval. In the following, we focus on the jets occurring at 06:13:47, 06:36:02, and 07:00:55 UT. These jets are referred to jet #1, jet #2, and jet #3 respectively. The jets' peak dynamic pressure is marked by vertical black lines. Figure 2e shows the ion energy spectrogram by the MMS FPI instrument. After the observation of jet #1 at 6:15 UT, the MMS1 spacecraft was briefly positioned inside the magnetosphere indicated by the change in the energy spectrogram and in the magnetic field. At 6:36 UT the plasma population transitioned from containing higher energy particles to lacking these high energy particles, this lasted until 6:55 UT. The time instance at 6:36 UT marked the change from the quasi-parallel to the quasi-perpendicular magnetosheath which coincided with jet #2. Jet #1 and jet #3 were not associated with such a change. Figure 2f shows the magnetic field inside the magnetosheath from the MMS1 spacecraft which was generally variable. In the quasi-perpendicular magnetosheath the magnetic field was less variable compared to the quasi-parallel magnetosheath (Luhmann et al., 1986).

Based on this data we estimated the footpoint for jets 1–3 according to the method outlined in Section 2.3. The footpoints are given in Table 2. The Dst index was −17, −22, and −22 nT for the three jets respectively.

Figures 2g–2i show the three magnetic field components (B_N, B_E, and B_Z respectively) from six ground magnetometer stations located close to or on Svalbard. These stations are located close to the estimated footpoints. The GMAG stations are Ny-Ålesund (NAL), Longyearbyen (LYR), Hopen Island (HOP), Bear Island (BJN), Hornsund (HRN), and Barentsburg (BBG). A 10 min time interval 190 s after the jets' peak dynamic pressure is marked in blue (190 s corresponds to the average propagation time of the jet observation to the ground (Norenius et al., 2021)). In red, we marked a 20 min time interval with low activity in the ground magnetic field which was used to compare the ground disturbance to the overall level of fluctuations. The largest amplitude was observed by the magnetometer stations on Hopen Island showing a disturbance of 125 nT, around 6:20 UT after jet #1. The amplitude of ground disturbance associated with jet #2 and jet #3 were lower.

Even though we focus on the ground disturbance of jet #1–3, Figure 2a shows several jets occurring shortly before and after jet #1 and 2. Wang et al. (2022) showed that recurrent jets cause a stronger ground disturbance. Especially jet #1 and jet #2 have other jets preceding and succeeding which could intensify to the ground disturbance. Since we cannot separate the contributions from different jets, we focus on jet #1 and jet #2. But the increased strength of the ground disturbance occurring after jet #1 and 2, might be the result of several jet impacts. Jet #3, however, is an isolated jet.

Figure 2j, shows estimates of the electric field E derived from SuperDARN measurements. The distance from the footpoint to the location of the estimate of E is shown in Figure 2k. We used the distance to footpoint 2 as an approximation for the distance to all footpoints since the footpoints of jet #1 and jet #3 were close to the footpoint of jet #2. We used estimates for the Pedersen conductance Σ_P using EISCAT data, the data are presented in Figure 2l.

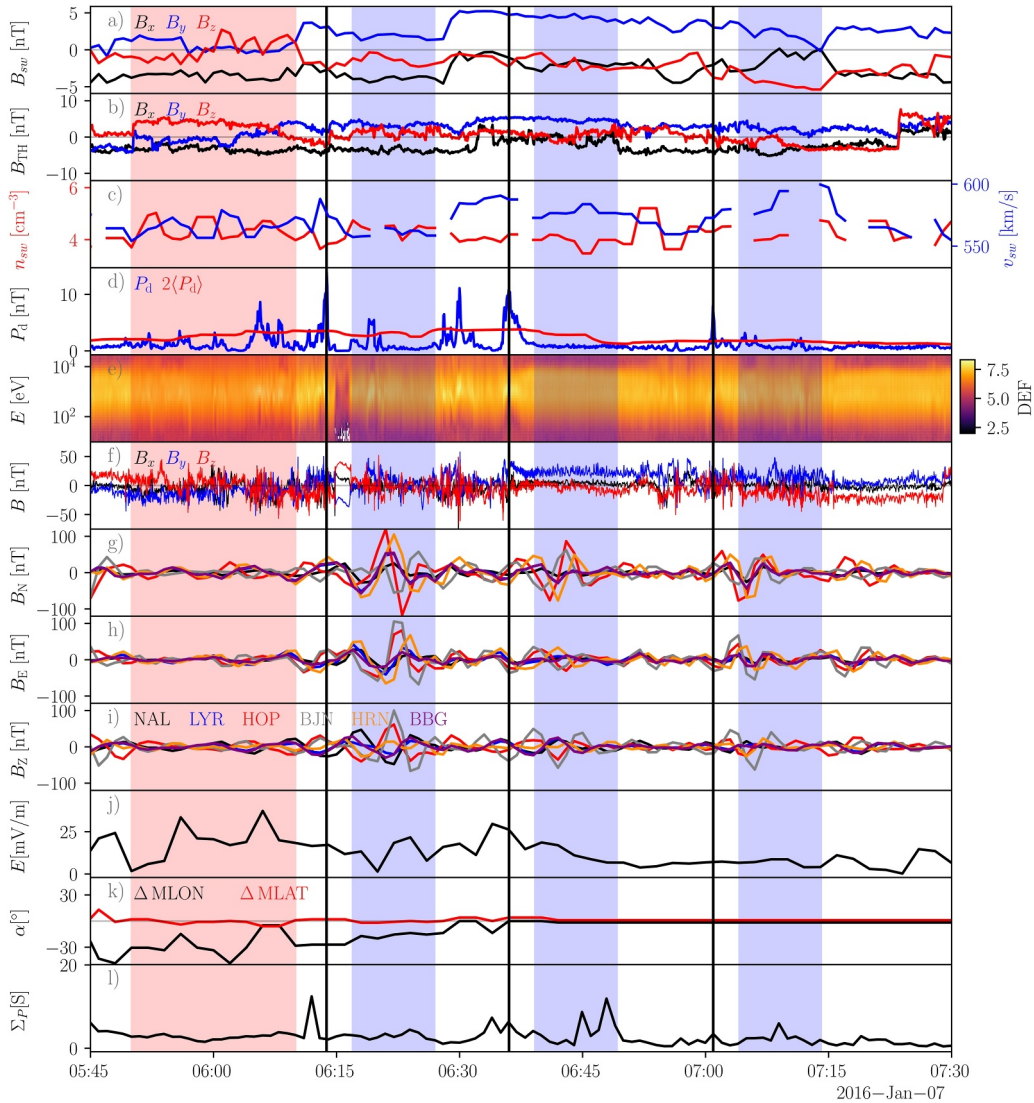

Figure 2. Overview of solar wind, magnetosheath and ground observations at 2016-01-07 05:45–07:30 UT. Three jets are marked by black vertical lines. (a) interplanetary magnetic field (IMF) propagated to the bow shock from the OMNI database, (b) IMF from the THEMIS C spacecraft, (c) the solar wind density (red) and velocity (blue) from the OMNI database, (d) Magnetospheric Multiscale (MMS) measurements showing the dynamic pressure (black) and the threshold for magnetosheath jets $2\langle P_d\rangle$ (red), (e) MMS ion energy spectrogram, (f) MMS magnetic field components, (g)-(i) magnetic field components (B_N, B_E, B_Z) from six magnetometer stations (NAL, LYR, HOP, BJN, HRN, and BBG) bandpass filtered between 1.67−6.67 mHz, (j) Electric field measurements E from SuperDARN, (k) difference in magnetic latitude and magnetic longitude from the SuperDARN measurement and the footpoint of jet #2, and (l) Pedersen conductance from EISCAT Svalbard measurements. The blue shaded areas correspond to 10 min intervals 190 s after each jet's peak dynamic pressure. The red shaded area is the quiet interval were there was little disturbance in the ground magnetic field in the Pc5 range. Solar wind and magnetosheath data are given in Geocentric solar magnetospheric coordinates.

Table 2
The Estimated Footpoints of Jet #1, Jet #2, and Jet #3 in Both Geographic and Magnetic Coordinates As Well As the Time of Their Peak Dynamic Pressure Observation

Jet no.	Time [UT]	GLAT [°]	GLON [°]	MLAT [°]	MLON [°]	MLT [°]
1	06:13:47	75.8	28.8	72.6	115	9.10
2	06:36:02	74.5	24.6	71.4	110	8.79
3	07:00:56	75.2	32.2	71.8	117	9.23

During the time interval 05:45–07:30 UT, there was no geomagnetic storm activity in the magnetosphere, the Dst index was low. Around 07:10 UT the expansion phase of a substorm started (data not shown), coinciding with the ground disturbance of our last jet. The average auroral electrojet (AE) index (Davis & Sugiura, 1966; Nose et al., 2015a) was around 100 nT between 06:15–07:10 UT and increased to around 400 nT until 07:30 UT. Since substorms mainly affect the nightside ionosphere while our events mainly impact the dayside ionosphere, we do not expect the substorm to affect our results. Furthermore, the substorm starts at 07:10 UT, so after the peak ground response of jet #3 (around 07:03 UT). The overlap between the two events is therefore short. Even though Nykyri et al. (2019) suggested a jet-triggered substorm, the authors argued that the jet only provided the final flux enhancement to trigger the onset of reconnection. The remaining flux was added during a prolonged period of southward IMF prior to the jet occurrence. The energy released during a jet-triggered substorm should therefore not be attributed solely to the jet itself. In summary, we argue that there was no significant magnetospheric activity that could cause the observed Pc5 activity in the GMAGs on the dayside (see Figures 2g–2i).

The three jets highlighted in Figure 2 show different features and can be classified into different categories following Raptis et al. (2020). Jet #1 and 3 were embedded in the quasi-parallel magnetosheath and were therefore quasi-parallel jets. Jet #1 was in addition associated with magnetopause movement as observed in Figure 2e at 06:15 UT in the MMS1 ion energy spectrogram. Jet #2 was a boundary jet since it is observed between the quasi-parallel and quasi-perpendicular magnetosheath associated with a rotation in the IMF which occurred around 6:30 UT (see Figures 2a and 2b). The IMF changed from $B_x < 0$ to $B_x \approx 0$, and B_y increased. This IMF orientation lasted until 6:50 UT when B_x and B_y decreased, this change was more pronounced in the THEMIS data (Figure 2b).

In the following paragraphs, we discuss the spatial extent of the ground perturbations in more detail. We investigated the perturbations' variation along approximately constant latitude (Figure 3a) and along approximately constant longitude (Figure 3b) as defined in Section 2.3. The black vertical lines represent again the jets' peak dynamic pressure (same as in Figure 2). The data were also band-pass filtered between $1.67 - 6.67$ mHz. We do not show all stations that fit the criteria of approximately constant latitude or longitude, since some perturbations are overlapping with other stations. In order to discuss the ground perturbations we use two station sets: *affected stations* and *significantly affected stations*. *Affected stations* refer to stations were the ground perturbation is measurable. Since the magnetic perturbation, and therefore the energy dissipation, is small in stations far away from the maximum disturbance we define a subset of *significantly affected stations*. In our events, all affected stations are located on the dawnside since none of the stations on the duskside satisfy the criteria for an affected stations. Due to the sparse magnetometer coverage on the duskside we do not know how or if the signal propagated on the duskside.

To determine all affected stations, we compared the maximum disturbance (blue areas in Figure 3) to quiet conditions (red area in Figure 3). First, we determined the maximum disturbance in the magnetic field magnitude during the quiet time interval (2016-01-07 05:50–06:10 UT, marked in red in Figure 3) denoted $B_{\mathrm{max,quiet}}$ for each station. We then calculated the maximum magnetic field magnitude $B_{\mathrm{max,jet}}$ in a 10 min interval 190 s after the jets' peak dynamic pressure (marked in blue in Figure 3). Finally, we compared $B_{\mathrm{max,quiet}}$ to $B_{\mathrm{max,jet}}$ and stations were considered to show a jet-triggered signature if $B_{\mathrm{max,jet}} > 2\ B_{\mathrm{max,quiet}}$.

Along approximately constant latitude (Figure 3a), we found that jet #1 affected 14 stations (KUV, UPN, GDH, ATU, STF, SKT, DMH, NAL, LYR, JAN, HOP, BJN, HRN, BBG). These stations spanned 5.1 hr in MLT, corresponding to 77° in longitude. Jet #2 affected 6 stations (KUV, SKT, JAN, HOP, BJN, HRN), spanning the same longitudinal range. Jet #3 affected 10 stations (CBB, KUV, GDH, ATU, STF, SKT, DMH, JAN, HOP, BJN). We neglected the station CBB since the magnitude pertubation was low and therefore not likely connected to the jet itself. Jet #3 also spanned 5.1 hr in MLT.

Figure 3b shows variations along approximately constant longitude sorted by MLAT (northernmost station on the top). The perturbation first increased in amplitude until the stations Hornsund (HRN), Hopen Island (HOP), and Bear Island (BJN). Stations south of these aforementioned stations showed a decrease in amplitude. The perturbation after jet #1 affected stations between NAL and MNK. Jet #2 affected stations between HRN and HAN and jet #3 affected stations between HOP and MNK. The perturbation might have even propagated to lower magnetic latitudes, but due to the sparsity of magnetometers and the low amplitude, we did not investigate this further.

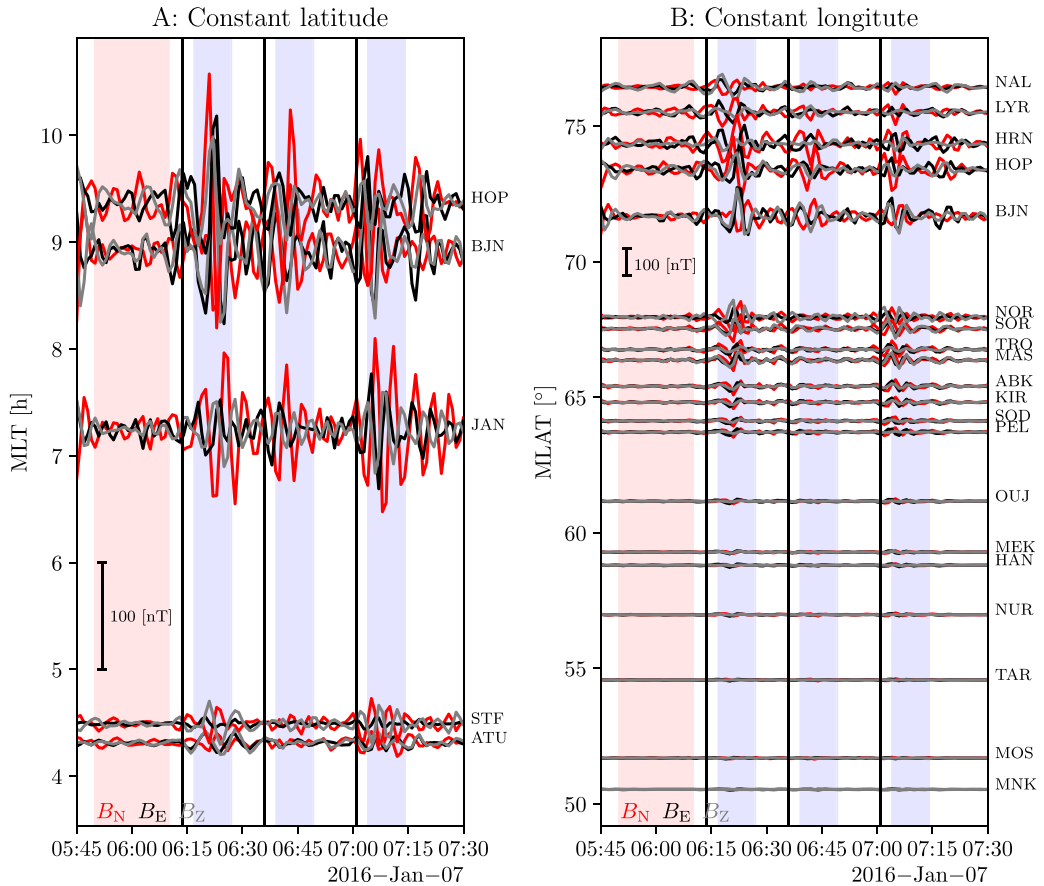

Figure 3. Ground response due to jet impact presented in a stackplot. (a) Measurements from different stations along constant latitude sorted by magnetic local time. The stations HRN, KUV, UPN, NAL, DMH, CBB, BBG, GDH, LYR, and SKT were excluded for visualization purposes since they were in close proximity to other stations and their perturbations were overlapping, (b) measurements from SuperMAG stations along constant longitude sorted by magnetic latitude from north to south. Here the stations BBG, SPG, MUO, LOZ, NR2, KEY, and IVA were excluded for the same reason as above. The red and the blue areas are the same as in Figure 2. The red area corresponds to the quiet interval that was chosen to compute the maximum disturbance $B_{max,pre}$ that was used as a threshold. The time intervals marked in light blue correspond to the time intervals were the maximum disturbance of the wave was computed $B_{max,jet}$. Stations were considered to be affected where $B_{max,jet} > 2\ B_{max,pre}$.

For each jet, the affected stations and footpoints are shown on a global map, see Figure 4. The footpoint of each jet is marked in red. The affected stations along approximately constant latitude are marked in white and in yellow for approximately constant longitude. We also modeled the footarea by assuming that the jet's impact diameter is the observed scale size, which is shown in orange. The observed scale size was calculated by integrating the velocity during the jet observation. Assuming the impact diameter to be the observed scale size implies a simple geometric structure for jets. Fatemi et al. (2024), however, showed that jet structures are more complicated. But, due to the proximity of the four MMS spacecraft we were not able to determine the shape of the investigated jets in another way. The modeled footarea is $6.5 \cdot 10^{10}$ m^2 for jet #1, $2.6 \cdot 10^{10}$ m^2 for jet #2, and $2.8 \cdot 10^{10}$ m^2 for jet #3.

To estimate the observed footarea we used the information on the latitudinal and longitudinal propagation. We were only interested in the stations with a significant signal. Stations with small disturbances would likely not play a significant role in the energy dissipation. The sparse distributions of magnetometers, especially along approximately constant latitude, introduced additional uncertainties in the observed footarea. Since we did not know the shape of the observed footarea due to the sparse sampling, we assumed that the footarea can be represented by a latitude-longitude rectangle.

We determined a subset of significantly affected stations from our list of affected stations to estimate the observed footarea. We calculated the maximum amplitude B_{max} of each station during the 10 min interval used previously.

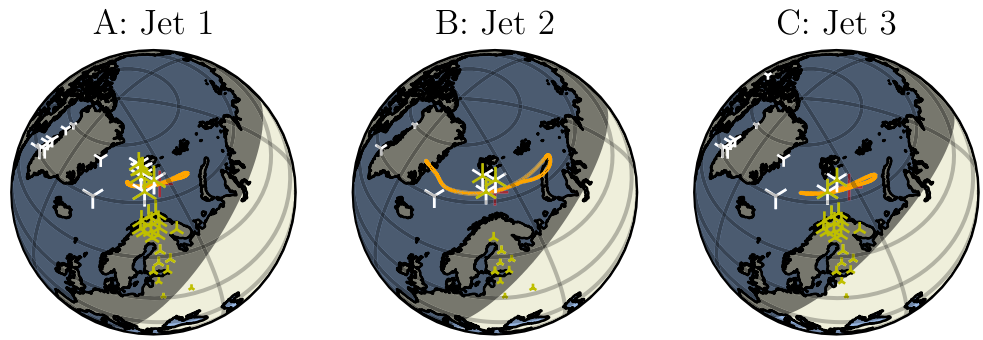

Figure 4. The spatial distribution of the affected stations for each jet. The estimated footpoints are given in red, and the modeled footarea is given in orange. Stations along approximately constant latitude are given in white and stations along approximately constant longitude are give in yellow. The size of the respective marker indicates the magnitude of the largest disturbance. The grid represents the CGM coordinate system.

Then we determined the station with the maximum disturbance from all stations denoted $B_{\max,\max}$. We considered a station to be significantly affected when $B_{\max} > B_{\max,\max}/3$.

For jet #1, the stations between JAN and HOP were significantly affected along approximately constant latitude covering 2.1 hr in MLT. Along approximately constant longitude stations between SOR and NAL were affected covering 8.8° in MLAT. The resulting observed footarea A_{obs} is $1.1 \cdot 10^{12}$ m^2. The same stations were affected for jet #2 as for jet #1 along approximately constant latitude. Along approximately constant longitude the stations between HRN and BJN were affected covering 2.6° in MLAT. A_{obs} was $3.0 \cdot 10^{11}$ m^2. For jet #3 the same stations as for jet #1 and 2 were affected along approximately constant latitude. Along approximately constant latitude stations between MAS and HOP were affected covering 6.9° in MLAT. A_{obs} was therefore $9.2 \cdot 10^{11}$ m^2. These results are summarized in Table 3.

4. Energy Deposition

4.1. Joule Heating

With the estimated footarea for jet #2 and 3 we calculated the energy dissipation in the ionosphere due to Joule heating. However, we did not make an estimate on the Joule heating for jet #1 due to the large distance between the footpoint and the measurement taken by SuperDARN (Figure 2k). The electric field measurement and jet #1 were likely not related due to the large distance. We therefore only estimated the Joule heating rate and the resulting energy dissipation for jet #2 and jet #3. Our estimates are also included in Table 3.

Table 3
Modeled and Observed Parameters Used to Estimate the Joule Heating in the Ionosphere

	Jet #1	Jet #2	Jet #3
ΔMLT [h]	2.1	2.1	2.1
ΔMLAT [°]	8.8	2.6	6.9
A_{obs} [m^2]	$1.1 \cdot 10^{12}$	$3.0 \cdot 10^{11}$	$9.2 \cdot 10^{11}$
A_{mod} [m^2]	$6.5 \cdot 10^{10}$	$2.6 \cdot 10^{10}$	$2.8 \cdot 10^{10}$
E $\left[\frac{\text{mV}}{\text{m}}\right]$	-	12	6.5
$\Sigma_p[S]$	-	4.2	2.5
S [mW/m^2]	-	0.65	0.11
Q_{obs} [J]	-	$1.2 \cdot 10^{11}$	$6.1 \cdot 10^{10}$
Q_{mod}[J]	-	$1.0 \cdot 10^{10}$	$1.9 \cdot 10^{9}$

Note. ΔMLT are the significantly affected stations along approximately constant longitude, ΔMLAT were the significantly affected stations along approximately constant latitude, A_{obs} is the observed footarea, A_{mod} is the modeled footarea, E is the electric field, Σ_p is the conductance, S is the Joule heating rate, Q_{obs} is the estimated Joule heating using A_{obs}, and Q_{mod} is the estimated Joule heating using A_{mod}.

We computed a 10 min average of the Pedersen conductance and electric field, 190 s after the observation of the jet's peak dynamic pressure (marked in blue in Figure 2). For jet #2, we found $E = 12$ mV/m and $\Sigma_p = 4.2$ S. This resulted in a Joule heating rate of 0.65 mW/m^2. For jet #3, we found $E = 6.5$ mV/m and $\Sigma_p = 2.5$ S. This resulted in a Joule heating rate of 0.11 mW/m^2. The total energy dissipated was estimated by integration over the affected area and time. The observed wave on the ground was damped and we assumed that the wave activity lasted 10 min.

We made two estimates for the footarea, the observed and modeled footarea. The modeled footarea is expected to be smaller since it does not take into account azimuthal wave propagation from the impact area at the magnetopause. To estimate the energy dissipation we assumed a constant Joule heating rate over the entire affected area. Using the observed footarea this resulted in a energy deposition of $1.2 \cdot 10^{11}$ J for jet #2 and $6.1 \cdot 10^{10}$ J for jet #3. Using the modeled footarea the energy deposition was $1.0 \cdot 10^{10}$ J for jet

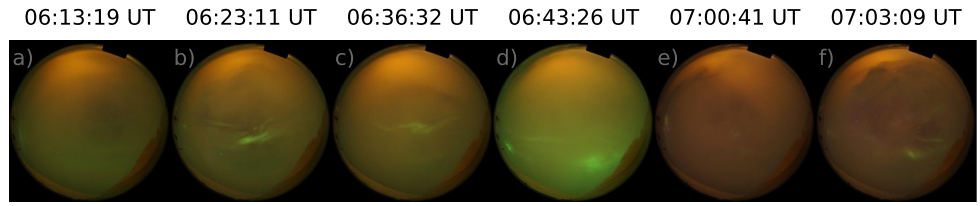

Figure 5. Images from an all-sky camera located at the Kjell Henriksen Observatory on Svalbard. The images were taken before the increased ultralow frequency (ULF) wave activity (a,c,e) and during the increased ULF activity (b,d,f) of each jet.

#2 and $1.9 \cdot 10^9$ J for jet #3. Due to smaller estimated footareas, the estimated energy deposition was an order of magnitude lower using the modeled footarea compared to the observed footarea.

4.2. Auroral Precipitation

During the investigated time interval auroral activity was also present, see Figure 5, which potentially was an additional source of energy due to particle precipitation. Figure 5 shows six images from the Sony a7s All Aky Camera (ASC) located at the Kjell Henriksen Observatory (78.148°N, 16.043°E, 520 m altitude) on Svalbard. Each color image was taken with 4 s exposure time. Figure 5a shows the auroral activity before the ground-disturbance of jet #1 and Figure 5b shows auroral activity during the ground-response of jet #1. Figures 5c–5f show the auroral activity before and during ground-response for jet #2 (jet #3) respectively. Generally, there seems to be an increase in auroral emission intensity during increased Pc5 wave activity. However, the camera indicated that there was a changing cloud coverage which did not allow to draw any clear conclusions about the auroral evolution. Auroral brightening indicates additional energy input in the ionosphere. Due to the continuous change in cloud coverage, the correlation between the jet-triggered ULF waves and enhanced auroral precipitation was not well tested.

5. Discussion

We have investigated the ground-response of three jets with large scale sizes in detail. Specifically, we analyzed the magnetic disturbances on the ground and estimated the disturbed area on the ground (footarea) for three jets. Using the observed and modeled footarea we estimated the energy dissipation in the ionosphere due to Joule heating.

5.1. Estimates on Footarea

Before comparing the estimated energy input to other processes, we discuss our estimates for the observed and modeled footareas. The observed footarea was an order of magnitude larger than the modeled footarea for all jets (see Figure 4). Since we did not have information about the actual impact area of the jet on the magnetopause, both estimate are associated with uncertainties.

The data indicated that the amplitude of the ULF waves were decreasing with decreasing latitude along approximately constant longitude. The damped amplitude indicates either Alfvén waves launched directly through the magnetopause impact or a compressional wave propagating radially toward Earth. The amplitude of the ULF waves were also decreasing along approximately constant latitude away from the modeled footpoint (in the azimuthal direction). Together with the larger observed footarea than expected by the model, this indicates azimuthally traveling waves. Waves traveling azimuthally and radially in the magnetosphere couple to Alfvén waves traveling along magnetic field lines into the ionosphere which can then observed with magnetometers. This coupling transfers energy from the radial or azimuthal wave to the field aligned wave which can be observed as a damped disturbance on the ground.

The propagation of waves radially and azimuthally caused an observed footarea larger than the one expected by the magnetopause impact area. The observed footarea however could overestimate the actual energy dissipation in the ionosphere since the wave amplitudes were damped. The damping resulted in smaller disturbances, and therefore smaller energy input in the ionosphere, in locations far away from the largest disturbance. We partially mitigated this effect by only selecting stations that were significantly affected. More realistically, the Joule heating rate should be determined as a function of location, however, this would require better coverage of the

instruments. We will continue this discussion using the energy deposition derived with the observed footarea which can be seen as an upper limit for the energy dissipation.

There are differences in the ground signature of the three investigated jets. The disturbance with the highest amplitude was observed after jet #1 which was also the jet with highest dynamic pressure. Considering that the magnetopause briefly moved over the spacecraft after the observation of jet #1, it was likely that jet #1 caused the largest movement of the magnetopause which subsequently caused the disturbance with the highest amplitude on the ground. The Joule heating in the ionosphere for jet #1 would have been likely higher compared to jet #2 and jet #3.

Another interesting observation was that jet #2 had the largest scale size but the observed footarea was the smallest and with the smallest amplitude. Jet #2 was also a boundary jet. One complication was that we cannot determine the dynamic density profile of the jet with one-point measurements. The spacecraft might have not moved through the largest extent of the jet which resulted in a smaller estimate for the scale size. Whether different types of jets cause different ground signatures needs to be investigated statistically and is outside the scope of this study.

5.2. Estimates on Energy Deposition

The energy deposition and Joule heating rate for jet #2 and jet #3 are different which indicates that energy input from jets is variable. The Joule heating rate is nearly six times higher for jet #2 than for jet #3 leading to a greater energy deposition. This discrepancy arises from the smaller electric field and Pedersen conductance for jet #3, both of which are approximately half the values observed for jet #2. Although there are no observational data available to fully explain these differences, we can speculate about potential causes. One possible reason could be the presence of jets preceding jet #2, which may have intensified the disturbance, similar to the stronger ULF waves observed after recurring jets (Wang et al., 2022). Additionally, due to the small spacecraft separation between the MMS spacecraft, we could not observe the dynamic pressure profile or the spatial extent of jets. The extent and dynamic pressure profile affects the extent and magnitude of the impact at the magnetopause, which, in turn, affects the electric field amplitude in the ionosphere. To investigate this point further, future research needs to focus on obtaining conjunction events between different mission (e.g., THEMIS) or obtain events during special campaigns that can provide observations across larger spatial scales. Finally, auroral activity is known to change the local ionization and therefore the Pedersen conductance (Robinson et al., 1987). The ongoing auroral activity on the dayside could change the local Pedersen conductance and therefore the Joule heating rate.

We also compare the derived Joule heating in the ionosphere to other processes in the magnetosphere-ionosphere system. We found that the net Joule heating rate was 0.65 mW/m^2 and 0.11 mW/m^2 for jet #2 and jet #3 respectively using the values for the observed footarea. For those two jets the average Joule heating rate was 0.38 mW/m^2 and the average energy deposition is $9 \cdot 10^{10}$ J which should be seen as an upper limit. In comparison, Rae et al. (2007) found a net Joule heating rate of $0.40 - 0.48$ mW/m^2 in their global FLR event, which is similar to our results. Their ULF wave showed a peak-to–peak amplitude of 150 nT on the ground which is also comparable to ours. We therefore argue that our estimates for the Joule heating rate are reasonable.

In order to make a comparison of the energy dissipation between the event investigated by Rae et al. (2007) and the energy input of jets one needs to take into account the footarea and duration in both events. The event investigated by Rae et al. (2007) had a duration of at least 3 hr, possibly 8 hr while the ground response of a jet lasted 10 min. To make a valid comparison between the events, one needs to take into account that under optimal conditions up to 8 geoeffective jets impact on the magnetopause per hour (Plaschke et al., 2016). Assuming that 37% of the impacting jets trigger a ULF wave (Wang et al., 2022), there are 3 jet-triggered ULF waves per hour. This would dissipate $8.1 \cdot 10^{11}$ J over 3 hours while Rae et al. (2007) found an energy input of $4.3 \cdot 10^{14}$ J. Differences are both in the duration and in the footarea. Rae et al. (2007) found their event covered at least 65° in longitude and 10° in latitude, which is indeed similar to our observed footarea from observations. However, we used a smaller footarea to calculate the energy input since we argued that small disturbances far away from the main impact will not have a significant contribution to the energy input into the ionosphere. This argument is supported by the fact that the electric field observed with the SuperDARN radars is also confined to a smaller area (data not shown), suggesting that only a smaller area was significantly affected. Assuming that 3 jets impact over an hour indicates that the energy input is not continuous as in the event investigated by Rae et al. (2007).

Therefore, the smaller footarea and shorter duration lead to a much smaller energy input in the ionosphere when averaged over time.

In the time interval investigated here, the IMF was highly variable. Jets are more often observed downstream of the quasi-parallel bow shock and the occurrence rate is enhanced when the IMF is stable (Archer et al., 2013). Quasi-stable, quasi-parallel IMF conditions could be used to determine the maximum energy input into the ionosphere. Possibly, jets could drive continuous ULF waves under such conditions by continuously impacting the magnetopause. However, such events have not been reported. Nevertheless, these jets would likely affect a small footarea which results in a smaller energy input compared to the event investigated by Rae et al. (2007).

Joule heating plays an important role during substorms with 56% of the total energy dissipated in the ionosphere which corresponds to $23.2-61.4\cdot10^{14}$ J in total (Østgaard et al., 2002). Often, an empirical relationship between the auroral electrojet index AE and the Joule heating rate of the form $a\mathrm{AE}+b$ is used (see Østgaard et al., 2002, for an overview). Using $a=0.21\cdot10^{9}$ GW/nT and $b=1.8\cdot10^{9}$ GW from Richmond et al. (1990) and AE = 112 nT during the interval of interest (06:15–07:15 UT), this results in a Joule heating rate of $2.53\cdot10^{10}$ W. During an hour this results in an energy deposition of $9.11\cdot10^{13}$ J. The Joule heating from jets is therefore much smaller compared to the Joule heating from the auroral electrojets during substorms.

We observed an increased auroral activity together with the increased Pc5 wave activity. Auroral brightening due to jet impact has been described previously by Wang et al. (2018). The enhanced particle precipitation provides another source of energy input into the ionosphere. The appearance of discrete auroral arcs has been associated with FLRs previously (Samson et al., 1996). FLRs can cause parallel electric fields that accelerate electrons, potentially causing auroral arcs (Wei et al., 1994). A similar mechanism involving ULF waves could be responsible for setting up parallel electric fields that cause increased auroral displays upon jet impact on the magnetopause (Wang et al., 2018).

We argue that the energy dissipation in the ionosphere resulting from jets impacting the magnetopause is small compared to other relevant magnetospheric processes such as substorms and field line resonances. The main reason is the short duration and the small footarea of jets, while substorms are a phenomena on timescales of hours. We therefore conclude that Joule heating through ULF waves caused by jets do not play a significant role in the time-averaged energy budget of the magnetosphere. Even though we were not able to provide an estimate of the energy deposition from particle precipitation, similar arguments can be used in this case. For particle precipitation, field-aligned currents are needed which are potentially set up by ULF waves. Ultralow frequency waves caused by jets are short-lived and spatially confined which means that particle precipitation should also be short-lived and spatially confined.

Magnetosheath jets are one of many dayside transient phenomena that can dissipate energy in the ionosphere-magnetosphere system (Zhang et al., 2022). For example, hot flow anomalies can also trigger Pc5 oscillations on the ground (Wang et al., 2024). Šafránková et al. (2012) found a hot flow anomaly that caused a magnetopause deformation of 9 R_E. The Joule heating rate caused by other dayside transients could be larger compared to magnetosheath jets, especially transients with larger scale sizes causing larger magnetopause deformations. These transients could therefore have momentarily larger energy dissipation rates and affect larger areas compared to magnetosheath jets. However, their transient nature makes their duration short and the total effect probably small compared to the FLR event studied by Rae et al. (2007).

6. Summary

In this study, we provided the first estimate of the energy deposition in the ionosphere through jet-triggered ULF waves. We argued that jet-triggered particle precipitation and Joule heating through jet-triggered ULF waves, while momentarily significant, do not play a significant role in magnetospheric-ionospheric energy budget averaged over time. This is primarily due to the short duration and limited foot area of these transient events. In order to assess the energy deposition in the coupled ionospheric-magnetospheric system, estimates on the energy transferred through other jet-triggered processes should be added. Such processes are for example, impulsive penetration (Gunell et al., 2012; Karlsson et al., 2012) and bursty reconnection triggered by jets (Hietala et al., 2018). These processes can transfer energy through other mechanisms than ULF waves. Investigating these processes would make it possible to fully evaluate the relevance of magnetosheath jets on the Earth's planetary environment.

In summary, in this study we made the following findings.

1. Ground perturbations cover a larger area on the ground than expected from the mapping of the jet's extent at the magnetopause to the ground. This indicates wave propagation in the magnetosphere and the perturbation is therefore detectable far away from the jet's footpoint.
2. The average Joule heating rate for the two investigated events was 0.38 mW/m. This Joule heating rate of jet-triggered ULF waves and field line resonances are comparable. Momentarily the energy dissipation can be locally significant.
3. The resulting average Joule heating in the ionosphere is $9 \cdot 10^{10}$ J per event.
4. During optimal conditions 8 geoeffective jets are expected to impact the magnetopause per hour and three of these jets cause ULF waves. That would result in a Joule heating of $2.7 \cdot 10^{11}$ J per hour.
5. Compared to other processes in the magnetosphere, the average energy deposition from jets is low. We therefore conclude that the energy deposition from jet-triggered ULF waves are not likely to play are significant role in the magnetospheric-ionospheric energy budget on average.
6. Enhanced particle precipitation is also expected to occur locally and does not significantly contribute to the energy budget on average.

Data Availability Statement

Magnetospheric Multiscale, OMNI, and THEMIS data is available for download for at the Heliophysics Data Application Programmer's Interface (HAPI) https://hapi-server.org/servers/. Supermag data is availbale at https://supermag.jhuapl.edu/. SuperDARN data is available at https://superdarn.ca/. EISCAT data can be downloaded from the National Institute of Polar Research (NIPR) at http://pc115.seg20.nipr.ac.jp/www/eiscatdata/. ASC data is available at Krämer (2024). The Dst and AE indices are available from the WDC for Geomagnetism, Kyoto at https://wdc.kugi.kyoto-u.ac.jp/wdc/Sec3.html.

Acknowledgments
We acknowledge the use of MMS data available under https://lasp.colorado.edu/mms/sdc/public/. We acknowledge use of NASA/GSFC's Space Physics Data Facility's OMNIWeb service, and OMNI data available at https://omniweb.gsfc.nasa.gov/. We acknowledge NASA contract NAS5-02099 and V. Angelopoulos for use of data from the THEMIS Mission. Specifically: K. H. Glassmeier, U. Auster and W. Baumjohann for the use of FGM data provided under the lead of the Technical University of Braunschweig and with financial support through the German Ministry for Economy and Technology and the German Center for Aviation and Space (DLR) under contract 50 OC 0302. For the ground magnetometer data we gratefully acknowledge: INTERMAGNET, Alan Thomson; CARISMA, PI Ian Mann; CANMOS, Geomagnetism Unit of the Geological Survey of Canada; The S-RAMP Database, PI K. Yumoto and Dr. K. Shiokawa; The SPIDR database; AARI, PI Oleg Troshichev; The MACCS program, PI M. Engebretson; GIMA; MEASURE, UCLA IGPP and Florida Institute of Technology; SAMBA, PI Eftyhia Zesta; 210 Chain, PI K. Yumoto; SAMNET, PI Farideh Honary; IMAGE, PI Liisa Juusola; Finnish Meteorological Institute, PI Liisa Juusola; Sodankylä Geophysical Observatory, PI Tero Raita; UiT the Arctic University of Norway, Tromsø Geophysical Observatory, PI Magnar G. Johnsen; GFZ German Research Centre For Geosciences, PI Jürgen Matzka; Institute of Geophysics, Polish Academy of Sciences, PI Anne Neska and Jan Reda; Polar Geophysical Institute, PI Alexander Yahnin and Yarolav Sakharov; Geological Survey of Sweden, PI Gerhard Schwarz; Swedish Institute of Space Physics, PI Masatoshi Yamauchi; AUTUMN, PI Martin Connors; DTU Space, Thom Edwards and PI Anna Willer; South Pole and McMurdo Magnetometer, PI's Louis J. Lanzarotti and Alan T. Weatherwax; ICESTAR; RAPIDMAG; British Artarctic Survey; McMac, PI Dr. Peter Chi; BGS, PI Dr. Susan Macmillan; Pushkov Institute of Terrestrial Magnetism, Ionosphere and Radio Wave Propagation (IZMIRAN); MFGI, PI B. Heilig; Institute of Geophysics, Polish Academy of Sciences, PI Anne Neska and Jan Reda; University of L'Aquila, PI M. Vellante; BCMT, V. Lesur and A. Chambodut; Data obtained in cooperation with Geoscience Australia, PI Andrew Lewis; AALPIP, co-PIs Bob Clauer and Michael Hartinger; MagStar, PI Jennifer Gannon; LISN PI Cesar Valladares; SuperMAG, PI Jesper W. Gjerloev; Data obtained in cooperation with the Australian Bureau of Meteorology, PI Richard Marshall. The authors acknowledge the use of SuperDARN data.

References

Alken, P., Thébault, E., Beggan, C. D., Amit, H., Aubert, J., Baerenzung, J., et al. (2021). International geomagnetic reference field: The thirteenth generation. *Earth Planets and Space*, *73*(1), 1–25.

Angelopoulos, V. (2009). *The themis mission*. Springer.

Archer, M., & Horbury, T. (2013). Magnetosheath dynamic pressure enhancements: Occurrence and typical properties. *Annales Geophysicae*, *31*(2), 319–331. https://doi.org/10.5194/angeo-31-319-2013

Archer, M., Horbury, T., Eastwood, J., Weygand, J., & Yeoman, T. (2013). Magnetospheric response to magnetosheath pressure pulses: A low-pass filter effect. *Journal of Geophysical Research: Space Physics*, *118*(9), 5454–5466. https://doi.org/10.1002/jgra.50519

Auster, H., Glassmeier, K., Magnes, W., Aydogar, O., Baumjohann, W., Constantinescu, D., et al. (2008). The themis fluxgate magnetometer. *Space Science Reviews*, *141*, 235–264. https://doi.org/10.1007/978-0-387-89820-9_11

Burch, J., Moore, T., Torbert, R., & Giles, B.-h. (2016). Magnetospheric multiscale overview and science objectives. *Space Science Reviews*, *199*, 5–21. https://doi.org/10.1007/978-94-024-0861-4_2

Burrell, A. G., van der Meeren, C., Laundal, K. M., & van Kemenade, H. (2023). aburrell/aacgmv2 [Dataset]. Version 2.6.3. *Zenodo*. Retrieved from https://doi.org/10.5281/zenodo.7621545

Case, N., & Wild, J. (2012). A statistical comparison of solar wind propagation delays derived from multispacecraft techniques. *Journal of Geophysical Research*, *117*(A2). https://doi.org/10.1029/2011ja016946

Chisham, G., Yeoman, T. K., & Sofko, G. (2008). Mapping ionospheric backscatter measured by the superdarn hf radars–part 1: A new empirical virtual height model. *Annales Geophysicae*, *26*(4), 823–841. https://doi.org/10.5194/angeo-26-823-2008

Davis, T. N., & Sugiura, M. (1966). Auroral electrojet activity index ae and its universal time variations. *Journal of Geophysical Research*, *71*(3), 785–801. https://doi.org/10.1029/jz071i003p00785

Escoubet, C. P., Hwang, K.-J., Toledo-Redondo, S., Turc, L., Haaland, S., Aunai, N., et al. (2020). Cluster and mms simultaneous observations of magnetosheath high speed jets and their impact on the magnetopause. *Frontiers in Astronomy and Space Sciences*, *6*, 78. https://doi.org/10.3389/fspas.2019.00078

Fatemi, S., Hamrin, M., Krämer, E., Gunell, H., Nordin, G., Karlsson, T., & Goncharov, O. (2024). Unveiling the 3d structure of magnetosheath jets. *Monthly Notices of the Royal Astronomical Society*, *531*(4), 4692–4713. https://doi.org/10.1093/mnras/stae1456

Fuselier, S. A. (1994). Suprathermal ions upstream and downstream from the earth's bow shock. *Geophysical Monograph Series*, *81*, 107–119. https://doi.org/10.1029/gm081p0107

Gjerloev, J. (2009). A global ground-based magnetometer initiative. *Eos, Transactions American Geophysical Union*, *90*(27), 230–231. https://doi.org/10.1029/2009eo270002

Gjerloev, J. (2012). The supermag data processing technique. *Journal of Geophysical Research*, *117*(A9). https://doi.org/10.1029/2012ja017683

Greenwald, R., Baker, K., Dudeney, J., Pinnock, M., Jones, T., Thomas, E., et al. (1995). Darn/superdarn: A global view of the dynamics of high-latitude convection. *Space Science Reviews*, *71*(1–4), 761–796. https://doi.org/10.1007/bf00751350

Group, S. D. V. W., Martin, C., Rohel, R., Kunduri, B., Pitzer, P., Khanal, K., et al. (2024). Superdarn/pydarn: Pydarn v4.0 [Dataset]. *Zenodo*. Retrieved from https://doi.org/10.5281/zenodo.10452339

Gunell, H., Nilsson, H., Stenberg, G., Hamrin, M., Karlsson, T., Maggiolo, R., et al. (2012). Plasma penetration of the dayside magnetopause. *Physics of Plasmas*, *19*(7), 072906. https://doi.org/10.1063/1.4739446

SuperDARN is a collection of radars funded by national scientific funding agencies of Australia, Canada, China, France, Italy, Japan, Norway, South Africa, United Kingdom and the United States of America. The authors acknowledge the use of PyDarn (Group et al., 2024). The authors thank the PI Dag Lorentzen and the observatory engineer Mikko Syrjäsuo for Sony image access and the instrument maintenance. Quicklook summary data are available at kho. unis.no, and individual images upon request. The authors acknowledge the use of EISCAT DATA. EISCAT is an international association supported by research organisations in China (CRIRP), Finland (SA), Japan (NIPR and ISEE), Norway (NFR), Sweden (VR), and the United Kingdom (UKRI). We acknowledge the use of the PyGeopack package available at https://github.com/mattkjames7/PyGeopack/. The authors would like to thank Michael Krämer for his support using and testing the T96 library in Fortran. E. Krämer and M. Hamrin were supported by Vetenskapsrådet (VR) dnr 2018-03623 and by the Swedish National Space Agency (SNSA) Grant 2022-00138. H. Gunell was supported by the SNSA Grant 2023-00208. S. Raptis was supported by the NASA DRIVE Science Center for Geospace Storms (CGS) under award 80NSSC22M0163, by the Magnetospheric Multiscale (MMS) mission of NASA's Science Directorate Heliophysics Division via subcontract to the Southwest Research Institute (NNG04EB99C) and by the National Science Foundation (NSF) Geospace Environment Modeling (GEM) program 2225463. Financial support was provided to Katie Herlingshaw by the Research Council of Norway under contract 343302. A. Schillings was supported by VR Grant 2021-06683.

Hietala, H., Partamies, N., Laitinen, T., Clausen, L. B., Facskó, G., Vaivads, A., et al. (2012). Supermagnetosonic subsolar magnetosheath jets and their effects: From the solar wind to the ionospheric convection. *Annales Geophysicae*, *30*(1), 33–48. https://doi.org/10.5194/angeo-30-33-2012

Hietala, H., Phan, T., Angelopoulos, V., Oieroset, M., Archer, M. O., Karlsson, T., & Plaschke, F. (2018). In situ observations of a magnetosheath high-speed jet triggering magnetopause reconnection. *Geophysical Research Letters*, *45*(4), 1732–1740. https://doi.org/10.1002/2017gl076525

Hughes, W., & Southwood, D. (1976). The screening of micropulsation signals by the atmosphere and ionosphere. *Journal of Geophysical Research*, *81*(19), 3234–3240. https://doi.org/10.1029/ja081i019p03234

Karlsson, T., Brenning, N., Nilsson, H., Trotignon, J.-G., Vallières, X., & Facsko, G. (2012). Localized density enhancements in the magnetosheath: Three-dimensional morphology and possible importance for impulsive penetration. *Journal of Geophysical Research*, *117*(A3). https://doi.org/10.1029/2011ja017059

Kessel, R. L. (2008). Solar wind excitation of pc5 fluctuations in the magnetosphere and on the ground. *Journal of Geophysical Research*, *113*(A4). https://doi.org/10.1029/2007ja012255

Krämer, E. (2024). All-sky camera images from Kjell Henriksen observatory (svalbard) on January 7th, 2016 05:45-07:30 UT [Dataset]. *Zenodo*. Retrieved from https://doi.org/10.5281/zenodo.14222498

Krämer, E., Koller, F., Suni, J., LaMoury, A. T., Pöppelwerth, A., Glebe, G., et al. (2025). Jets downstream of collisionless shocks: Recent discoveries and challenges. *Space Science Reviews*, *221*(1), 1–59.

Luhmann, J., Russell, C., & Elphic, R. (1986). Spatial distributions of magnetic field fluctuations in the dayside magnetosheath. *Journal of Geophysical Research*, *91*(A2), 1711–1715. https://doi.org/10.1029/ja091ia02p01711

Mailyan, B., Munteanu, C., & Haaland, S. (2008). What is the best method to calculate the solar wind propagation delay? *Annales Geophysicae*, *26*(8), 2383–2394. https://doi.org/10.5194/angeo-26-2383-2008

Menk, F. W. (2011). Magnetospheric ulf waves: A review. *The Dynamic Magnetosphere*, 223–256. https://doi.org/10.1007/978-94-007-0501-2_13

Norenius, L., Hamrin, M., Goncharov, O., Gunell, H., Opgenoorth, H., Pitkänen, T., et al. (2021). Ground-based magnetometer response to impacting magnetosheath jets. *Journal of Geophysical Research: Space Physics*, *126*(8), e2021JA029115. https://doi.org/10.1029/2021ja029115

Nose, M., Iyemori, T., Sugiura, M., & Kamei, T. (2015a). Geomagnetic ae index. https://doi.org/10.17593/15031-54800

Nose, M., Iyemori, T., Sugiura, M., & Kamei, T. (2015b). Geomagnetic dst index. https://doi.org/10.17593/14515-74000

Nykyri, K., Bengtson, M., Angelopoulos, V., Nishimura, Y., & Wing, S. (2019). Can enhanced flux loading by high-speed jets lead to a substorm? Multipoint detection of the christmas day substorm onset at 08: 17 ut, 2015. *Journal of Geophysical Research: Space Physics*, *124*(6), 4314–4340. https://doi.org/10.1029/2018ja026357

Østgaard, N., Germany, G., Stadsnes, J., & Vondrak, R. (2002). Energy analysis of substorms based on remote sensing techniques, solar wind measurements, and geomagnetic indices. *Journal of Geophysical Research*, *107*(A9), SMP 9–1–SMP 9–14. https://doi.org/10.1029/2001ja002002

Papitashvili, N. E., & King, J. H. (2020). Omni 1-min data [Dataset]. *NASA Space Physics Data Facility*. https://doi.org/10.48322/45bb-8792. Accessed on 27 10 2022.

Picone, J., Hedin, A., Drob, D. P., & Aikin, A. (2002). Nrlmsise-00 empirical model of the atmosphere: Statistical comparisons and scientific issues. *Journal of Geophysical Research*, *107*(A12), SIA 15–1–SIA 15–16. https://doi.org/10.1029/2002ja009430

Plaschke, F., Hietala, H., & Angelopoulos, V. (2013). Anti-sunward high-speed jets in the subsolar magnetosheath. *Annales Geophysicae*, *31*(10), 1877–1889. https://doi.org/10.5194/angeo-31-1877-2013

Plaschke, F., Hietala, H., Angelopoulos, V., & Nakamura, R. (2016). Geoeffective jets impacting the magnetopause are very common. *Journal of Geophysical Research: Space Physics*, *121*(4), 3240–3253. https://doi.org/10.1002/2016ja022534

Plaschke, F., Hietala, H., Archer, M., Blanco-Cano, X., Kajdič, P., Karlsson, T., et al. (2018). Jets downstream of collisionless shocks. *Space Science Reviews*, *214*(5), 1–77. https://doi.org/10.1007/s11214-018-0516-3

Plaschke, F., Hietala, H., & Vörös, Z. (2020). Scale sizes of magnetosheath jets. *Journal of Geophysical Research: Space Physics*, *125*(9), e2020JA027962. https://doi.org/10.1029/2020ja027962

Pollock, C., Moore, T., Jacques, A., Burch, J., Gliese, U., Saito, Y., et al. (2016). Fast plasma investigation for magnetospheric multiscale. *Space Science Reviews*, *199*(1–4), 331–406. https://doi.org/10.1007/s11214-016-0245-4

Rae, I., Watt, C., Fenrich, F., Mann, I., Ozeke, L., & Kale, A. (2007). Energy deposition in the ionosphere through a global field line resonance. *Annales Geophysicae*, *25*(12), 2529–2539. https://doi.org/10.5194/angeo-25-2529-2007

Raptis, S., Karlsson, T., Plaschke, F., Kullen, A., & Lindqvist, P.-A. (2020). Classifying magnetosheath jets using mms: Statistical properties. *Journal of Geophysical Research: Space Physics*, *125*(11), e2019JA027754. https://doi.org/10.1029/2019ja027754

Richmond, A., Kamide, Y., Akasofu, S.-I., Alcaydé, D., Blanc, M., De la Beaujardière, O., et al. (1990). Global measures of ionospheric electrodynamic activity inferred from combined incoherent scatter radar and ground magnetometer observations. *Journal of Geophysical Research*, *95*(A2), 1061–1071. https://doi.org/10.1029/ja095ia02p01061

Robinson, R., Vondrak, R., Miller, K., Dabbs, T., & Hardy, D. (1987). On calculating ionospheric conductances from the flux and energy of precipitating electrons. *Journal of Geophysical Research*, *92*(A3), 2565–2569. https://doi.org/10.1029/ja092ia03p02565

Ruohoniemi, J., & Baker, K. (1998). Large-scale imaging of high-latitude convection with super dual auroral radar network hf radar observations. *Journal of Geophysical Research*, *103*(A9), 20797–20811. https://doi.org/10.1029/98ja01288

Russell, C., Anderson, B., Baumjohann, W., Bromund, K., Dearborn, D., Fischer, D., et al. (2016). The magnetospheric multiscale magnetometers. *Space Science Reviews*, *199*, 189–256. https://doi.org/10.1007/978-94-024-0861-4_8

Šafránková, J., Goncharov, O., Němeček, Z., Přech, L., & Sibeck, D. (2012). Asymmetric magnetosphere deformation driven by hot flow anomaly (ies). *Geophysical Research Letters*, *39*(15). https://doi.org/10.1029/2012gl052636

Samson, J., Cogger, L., & Pao, Q. (1996). Observations of field line resonances, auroral arcs, and auroral vortex structures. *Journal of Geophysical Research*, *101*(A8), 17373–17383. https://doi.org/10.1029/96ja01086

Shepherd, S. (2014). Altitude-adjusted corrected geomagnetic coordinates: Definition and functional approximations. *Journal of Geophysical Research: Space Physics*, *119*(9), 7501–7521. https://doi.org/10.1002/2014ja020264

Shue, J.-H., Chao, J.-K., Song, P., McFadden, J., Suvorova, A., Angelopoulos, V., et al. (2009). Anomalous magnetosheath flows and distorted subsolar magnetopause for radial interplanetary magnetic fields. *Geophysical Research Letters*, *36*(18). https://doi.org/10.1029/2009gl039842

Sugiura, M. (1963). Hourly values of equatorial dst for the igy. (Tech. Rep.). *NASA, Goddard Space Flight Center*. (No. NASA-TM-X-55238).

Tsyganenko, N. (1995). Modeling the earth's magnetospheric magnetic field confined within a realistic magnetopause. *Journal of Geophysical Research*, *100*(A4), 5599–5612. https://doi.org/10.1029/94ja03193

Tsyganenko, N. (1996). Effects of the solar wind conditions in the global magnetospheric configurations as deduced from data-based field models., *389*, 181.

Vuorinen, L., Hietala, H., & Plaschke, F. (2019). Jets in the magnetosheath: Imf control of where they occur. *Annales Geophysicae*, *37*(4), 689–697. https://doi.org/10.5194/angeo-37-689-2019

Wang, B., Liu, J., Han, D., Wang, Y., & Feng, X. (2024). Statistical study of hot flow anomaly induced ground magnetic ultra-low frequency oscillations. *Journal of Geophysical Research: Space Physics*, *129*(8), e2024JA032667. https://doi.org/10.1029/2024ja032667

Wang, B., Nishimura, Y., Hietala, H., & Angelopoulos, V. (2022). Investigating the role of magnetosheath high-speed jets in triggering dayside ground magnetic ultra-low frequency waves. *Geophysical Research Letters*, *49*(22), e2022GL099768. https://doi.org/10.1029/2022gl099768

Wang, B., Nishimura, Y., Hietala, H., Lyons, L., Angelopoulos, V., Plaschke, F., et al. (2018). Impacts of magnetosheath high-speed jets on the magnetosphere and ionosphere measured by optical imaging and satellite observations. *Journal of Geophysical Research: Space Physics*, *123*(6), 4879–4894. https://doi.org/10.1029/2017ja024954

Wannberg, G., Wolf, I., Vanhainen, L.-G., Koskenniemi, K., Röttger, J., Postila, M., et al. (1997). The eiscat svalbard radar: A case study in modern incoherent scatter radar system design. *Radio Science*, *32*(6), 2283–2307. https://doi.org/10.1029/97rs01803

Wei, C., Samson, J., Rankin, R., & Frycz, P. (1994). Electron inertial effects on geomagnetic field line resonances. *Journal of Geophysical Research*, *99*(A6), 11265–11276. https://doi.org/10.1029/94ja00582

Yeoman, T., Wright, D., Chapman, P., & Stockton-Chalk, A. (2000). High-latitude observations of ulf waves with large azimuthal wavenumbers. *Journal of Geophysical Research*, *105*(A3), 5453–5462. https://doi.org/10.1029/1999ja005081

Zhang, H., Zong, Q., Connor, H., Delamere, P., Facskó, G., Han, D., et al. (2022). Dayside transient phenomena and their impact on the magnetosphere and ionosphere. *Space Science Reviews*, *218*(5), 40. https://doi.org/10.1007/s11214-021-00865-0